International Journal of Design Engineering

ISSN online: 1751-5882 - ISSN print: 1751-5874
https://www.inderscience.com/ijde

Design exploration of a spring plate using FEM and Box-Behnken design

Dheeraj Gunwant

DOI: 10.1504/IJDE.2023.10053512

Article History:

Received:	11 December 2022
Last revised:	12 December 2022
Accepted:	23 December 2022
Published online:	05 July 2023

Design exploration of a spring plate using FEM and Box-Behnken design

Dheeraj Gunwant

Department of Mechanical Engineering,
Apex Group of Institutions,
Rampur, UP, India
and
Department of Mechanical Engineering,
Invertis University,
Bareilly, UP, India
Email: mailto.dheerajgunwant@gmail.com

Abstract: The current study aims at design exploration of a structural steel spring plate using FEM and design of experiments (DoE). Box-Behnken design (BBD) was used for DoE, and FEM was used to model and solve various design points. First, structural analyses of the spring plate were performed to determine the maximum deformation and von-Mises stress in the model. The study considered bend radius (P1), hole spacing (P6), and internal and external thicknesses (P11, P12) as input parameters. Twenty-five BBD-based numerical experiments were run in ANSYS WB. Regression analysis yielded accurate output parameter regression models based on input parameters. ANOVA was used to determine the importance of each input parameter on the output parameters. Response surface methodology (RSM) was used to determine the change in response variable vs. input parameters. The goodness-of-fit analysis showed good agreement between RSM-predicted and FEM-determined output parameters.

Keywords: fatigue analysis; design of experiments; DoE; response surface methodology; RSM; finite element analysis.

Reference to this paper should be made as follows: Gunwant, D. (2023) 'Design exploration of a spring plate using FEM and Box-Behnken design', *Int. J. Design Engineering*, Vol. 12, No. 1, pp.11–29.

Biographical notes: Dheeraj Gunwant obtained his Doctor of Philosophy from the G.B. Pant University of Mechanical Engineering, Pantnagar (Uttarakhand), India in 2018. He is presently the Director of Engineering at the Apex Group of Institutions, Rampur (Uttar Pradesh), India. His research areas include FEM, characterisation of composites and microwave-absorbing materials.

1 Introduction

Originating from the Latin word 'fatīgāre' meaning 'to tire', fatigue is defined as the alteration in the mechanical properties of a material due to the application of repeated loading. The term mainly applies to the changes leading to the ultimate cracking or failure of the material under such loading. Fatigue is a mysterious phenomenon due to its

uncertain nature and virtually invisible damage (Zenner and Hinkelmann, 2019). Repeated loading can initiate fatigue by nucleating minute cracks in material followed by their growth and failure. A machine component may undergo mechanical (Ertas and Sonmez, 2008), thermal (Lu et al., 2019), embrittling (Connolly et al., 2019), corrosion (Antunes et al., 2012), or fretting fatigue (Guo et al., 2020) based on fluctuations, thermal loading, chemically unstable environment, or reciprocating frictional contacts respectively. The durability and stability of a machine component define its stability to maintain its performance throughout its service life.

As indicated above, most industrial failures are related to fatigue. Fatigue is the slow wear of material under constant loading. It is often divided into three stages: crack initiation, propagation, and final fracture (Ertas and Sonmez, 2008). The total fatigue life is the sum of the number of loading cycles for fracture initiation and subcritical propagation to a final crack size. Fatigue is the primary cause of aeroplane, vehicle, welded structure, and machinery failure. Fatigue failure originates from non-metallic inclusions and microstructure defects, such as scratches, dents, and other manufacturing faults (Zerbst and Klinger, 2019). The columnar dendritic structure formed in welded zones by a high solidification rate also causes fatigue cracks. Similarly, welding and additive manufacturing is also known to produce inclusions and pores (Liu et al., 2019; Yang et al., 2020). For example, non-homogeneous microstructure with welded pores caused fatigue failure in welded titanium joints at 400ºC (Liu et al., 2021).

In a cast Al-Si alloy engine cylinder head, complex-shaped significant flaws were found as fatigue crack initiation spots (Ren et al., 2021). SEM study of the broken surface of laser-melted Ti alloy revealed fatigue cracks (Zhan, 2019). Surface-grain refinement improves the fatigue properties of metallic materials (Amanov et al., 2019; Maleki and Unal, 2018). Recently, computer technology has advanced rapidly. High-performance computing systems and continual software development have boosted numerical approaches like the FEM. FEM can model design modifications and get response function values with minimal divergence from actual values. FEM and design of experiments (DoE) let designers explore designs and find optimal engineering solutions.

Fatigue analysis was conducted to determine cemented implants' endurance using the Goodman, Soderberg and Gerber failure theories in ANSYS WB (Senalp et al., 2007). The analysis included four hip prosthetic forms with various curvatures. The simulation showed that all designs were safe under fatigue and static loads. Stem-3 constructed from Ti-6Al-4V was observed as most suitable for static and dynamic loadings. In addition, Guo et al. conducted a numerical analysis of the fatigue performance of ABS amphibious robot components (Guo et al., 2017). The fatigue life of these components was examined under cyclic loading to detect weak spots. Overall, design characteristics met fatigue life requirements.

Fatigue analysis has also been utilised for reducing an automobile's overall weight and the manufacturer's carbon footprint. The automobile's suspension system was analysed for stress distribution, fatigue life prediction, safety factor, and weight reduction (Ijagbemi et al., 2016). It was deduced that weight reduction with simultaneous better stability could be obtained using treated Ti-13V-11Cr-3Al for manufacturing the suspension system. The treated Ti-13V-11Cr-3Al suspension system displayed a safety factor of 1 under various loading scenarios. Fatigue life simulation of an automobile stabiliser bar under various road excitations has been reported by Li et al. (2019). Their simulation determined the ratio of simulated life to design life as 2.77 and 2.30, respectively. On the other hand, the simulated life cycles were obtained to be 2,710

compared to predicted life cycles of 3267, showing a deviation of just 17%. The lowest fatigue life was observed at the connection between the stabiliser bar body and sleeve due to the higher stress concentration at this location. Rubber components operating under varying cyclic loading play a vital role in the present industries. A FEM-based methodology for predicting the fatigue life of a natural rubber-filled cradle using the constitutive material behaviour and strain-life approach was reported (Zarrin-Ghalami and Fatemi, 2013). The predicted failure regions were in agreement with the experimentally observed failure regions. Springs find extensive applications in automobiles and industrial machinery and are generally subjected to dynamic loading. These complex loading scenarios, combined with various defects, viz. surface scratches, microstructural defects, inclusions, porosity and unpleasant environmental conditions, entail their catastrophic failure (Prawoto et al., 2008). In order to obtain weight reduction, a comparative failure analysis of steel and composite leaf springs was conducted by Kumar and Vijayarangan (2007). The composite leaf displayed up to 67.35% lower stress, 126.98% increase in the natural frequency, and 64.95% improved stiffness w.r.t. the conventional steel leaf-spring. Moreover, the composite leaf spring was 68.15% lighter, along with better fatigue strength than the conventional steel leaf spring. Valuable insight can be gained regarding the failure mechanisms via experimental tests and scanning electron microscopy of the fractured surfaces (Das et al., 2007). In addition, FEM has also emerged as a quick and easy tool for investigating fatigue failure problems (Zhu et al., 2014). Variable amplitude loading in vehicle suspension causes fatigue failure of the automobile springs. The variable amplitude loading signal collected from various road conditions was employed to determine the fatigue performance of parabolic leaf springs (Kong et al., 2014). The spring displayed the lowest fatigue strength during rough road conditions. However, their research suggested necessary modifications in the springs' parabolic geometry, especially while cornering. Twin torsion springs are used for vibration isolation in the clutch mechanisms. An FEA was conducted to assess the fatigue performance of medium-temperature tempered SUS 631 stainless steel (Zhang et al., 2021). The SEM study revealed noticeable shrinkage porosity in the fatigue extension zone in the fractured region. The experimental fatigue tests revealed the failure of samples after completing 1×10^5 to 1.1×10^5 cycles. Maximum von-Mises stress of 4,770.40 MPa was observed in the experimentally observed failure locations, establishing the FE model's validity.

The present paper investigates the fatigue behaviour of a structural steel spring plate under time-dependent loading conditions. The design exploration study was conducted via the DoE and response surface methodology (RSM) for four input and output parameters. First, numerical experimentations of fatigue analysis were performed using ANSYS WB for 25 design points obtained by the Box-Behnken methodology. Then, the regression analyses were performed on the results to obtain the input-output relationships. Next, analysis of variance (ANOVA) was performed to determine the percentage contribution of the input parameter to the output parameters. Finally, RSM contour plots were presented to aid the designer in selecting the input parameter values. The study presents a robust methodology for combining the FEM with DoE for various design challenges faced by engineers and scientists in this field.

2 FEM and DoE

DoE refers to selecting the values of independent variables in physical experimentation or numerical simulation with the intent of some objects in mind. The objective can be the development of a response surface for the phenomenon under observation and represented as a dependent variable. The response surface is typically a functional relationship between input and output expressed as a low-order polynomial. The designer can understand the input-output relationship by filtering unwanted noise via a surrogate model (Gianchandani and Crary, 1998). The shape optimisation problem in an automobile wheel through FEM and DoE was carried out by Schäfer and Finke (2008). They highlighted the drastic reduction in the number of experiments from 531,441 to 98 without and with DoE, respectively. On the other hand, without FEM, each trial would have required separate physical tools for performing the experiments. Figure 1 presents the general schematic of combining DoE with FEM to obtain optimal shapes for automobile wheels. Through this combination, they could save up to 1 kg mass per vehicle.

Figure 1 A general schematic of DoE and FEM techniques

Source: Schäfer and Finke (2008)

A systematic study using DoE and FEM on the influence of design parameters on the mechanical behaviour of metallic bellows has been reported by Prasanna Naveen Kumar et al. (2017). The mathematical relation was deduced through Box-Behnken design (BBD), and RSM was used to infer that the wall thickness was the most influential of all the factors. Investigations on the impact behaviour of helmets using FEM and DoE have been reported by Shuaeib et al. (2007). The BBD methodology was utilised to obtain the design matrix and simulate each design point through FEM. The foam thickness and density were the most influential factors in avoiding head injury. The most optimal design parameters obtained using the analysis were foam density of 55 kg/m^3, foam thickness of 15 mm and shell thickness of 5 mm. FEM and DoE have also been utilised for obtaining optimal design by selecting parameters for producing two identical sheet metal blanks on the same mould with good quality Al-Momani and Rawabdeh (2008). Combining these two methodologies has effectively reduced the experimental effort and cost. A systematic analysis was conducted for two types of steels, five clearances values, two blank holder force values and four sheet thicknesses amounting to 80 simulations. The simulations reveal a direct relationship between the burr height of the sheared edge and geometric characteristics, as well as material types. The burr height can be minimised by setting the clearance to 5% and no blank holder force. A 10-factor orthogonal DoE analysis was employed as an exploratory tool for identifying the critical factors in laser powder bed fusion FEA by Ma et al. (2015). A 3D thermal model with dimensions 6x1.4x0.6 mm^3 was created, comprising a single layer of metal powder (thickness = 37 μm) over a metal substrate. The order of dominant factors (affecting peak temperature by

≥2%) was identified as laser power > specific heat > laser scan speed > power packing ratio. FEM and DoE were utilised to investigate the influence of design variables on the chip surface temperature and cutting forces in the hot turning of Inconel 718 (Parida and Maity, 2016). Various design variables, viz., cutting speed, heating temperature, feed rate and constant depth of cut, were employed for analysing the responses. They reported a decrease in cutting force when the temperature was increased to 450ºC from room temperature. In another work, a combination of FEM with DoE was employed for predicting critical parameters in the rolling process via nonlinear 3D FE models (Bordonaro et al., 2018). Influence of input parameters: workpiece diameter, temperature, diameter reduction and angular velocity were investigated on the output parameters: workpiece spread, effective and contact stresses and reactions. The riveting process includes piercing joining plates through the mandrels on the rivet. These mandrels must be sufficiently stable to avoid buckling under a piercing load. At the same time, the mandrels must also be sufficiently soft to undergo self-flaring, avoiding using any particular tool. Such conflicting objectives were handled by combining FEM and DoE to obtain a suitable rivet geometry that can lance high-strength steel and undergo self-flaring (Kraus et al., 2020). Various parameters such as cross-sectional area, chamfer length, and top/bottom sheet thicknesses were considered in the analysis as input variables. Based on the analysis, the cross-sectional area was obtained as 3.2 mm^2 giving a self-flaring rivet-geometry with a minimum flaring of 0.3 mm. Thin-walled structures are essential in applications where weight reduction is imperative. Holes drilled in these structures can further reduce the weight and simultaneously provide recessions for repair and maintenance. The buckling performance of a thin-walled C-cross-section structure with holes was optimised through DoE and FEM (Bin Kamarudin et al., 2022). Parameters such as the spacing ratio, the shape of the hole, and the opening ratio were varied systematically to obtain the optimal critical buckling load. Using the DoE matrix and explicit FEA, Wei and Olatunbosun (2016) deduced the optimal relaxation length for the rubber wheel. Seven factors, including steel belt and carcass material properties, were evaluated at three levels, culminating in 15 numerical experiments. They observed a strong relationship between carcass cord spacing and cross-sectional area and elasticity, together with the crown angle and the relaxation length for the two steering input functions.

3 Methodology

3.1 Fatigue analysis

In the present investigation, the spring plate shown in figure was subjected to a load of 35 N in the negative Y-direction. In addition, fixed boundary conditions were applied to the holes to simulate the effect of bolted connections between the spring plate and the supporting structure. Figure 2(a) presents the CAD model of the spring plate displaying the loading and boundary conditions. The fatigue performance of the spring plate was evaluated under zero-based fatigue loading for an R-value of '0'. The FE model is divided into 265,894 tetrahedral finite elements, as shown in Figure 2(b). The mesh size near holes was refined to achieve good accuracy with high computational efficiency. The Goodman mean stress correction theory was employed for the mean stress correction (Pastorcic et al., 2019; Zhang et al., 2021). Figures 3(a) and 3(b) presents the graphical

representation of the load on the spring plate and Goodman's mean stress correction theory.

Figure 2 (a) CAD model of the spring plate showing the loading and boundary conditions (b) Meshed model (note the finer mesh near holes) (see online version for colours)

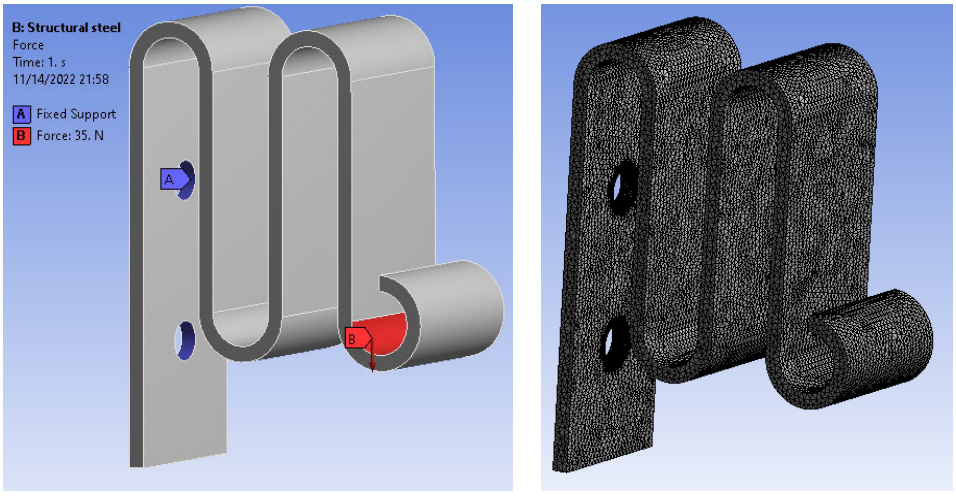

(a) (b)

Figure 3 Graphical representation of zero-based loading and Goodman mean stress correction theory (see online version for colours)

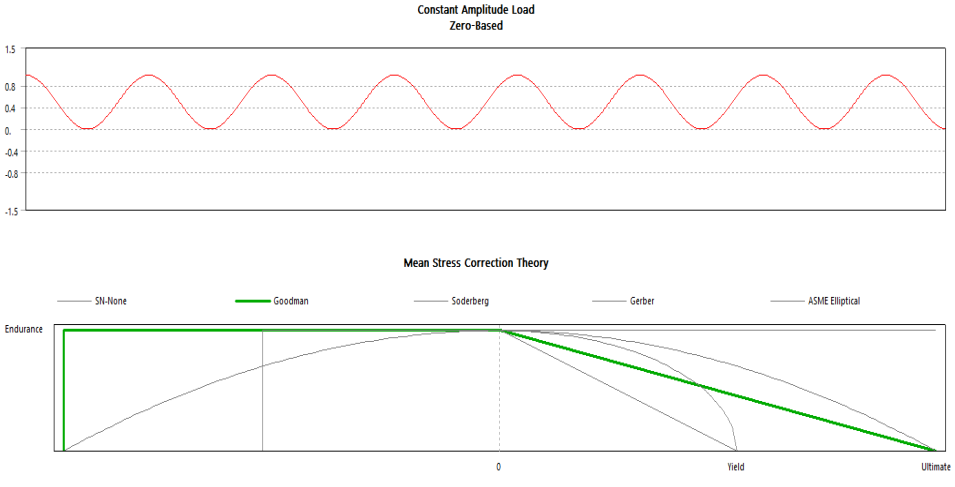

Figure 4 presents the S-N curve of structural steel. Its elastic properties are presented in Table 1.

Figure 4 SN curve for structural steel

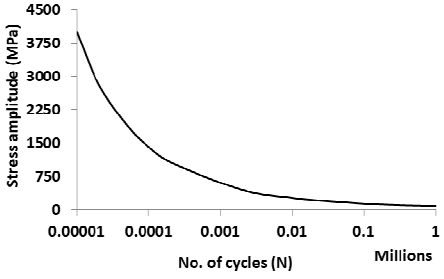

Table 1 Mechanical properties of structural steel

Parameter	*Structural steel*
Young's modulus (MPa)	205×10^3
Poisson's ratio	0.33
Tensile yield strength (MPa)	257
Tensile ultimate strength (MPa)	463

3.2 Box-Behnken design

In this study, the BBD methodology was employed for the design exploration of a spring plate. Figure 5 presents the CAD model of the spring plate showing the input parameters' initial, minimum and maximum values used in the analysis. The initial value was selected for initiating the design exploration. The input parameters were varied by ± 10% of the initial values to obtain various levels of design. The influence of input parameters on the output parameters was studied using this technique. The RSM is a statistical technique for obtaining linear (or quadratic) approximation surfaces from the available experimental/numerical data. It aids the designer in selecting the optimum design parameters. BBD is one of the DoE techniques used in RSM and requires fewer experimental points than the central composite design (CCD). The BBD is based upon the three-level fractional factorial design possessing the orthogonal (rotatable or nearly rotatable) design characteristics. The BBD methodology significantly reduces the number of numerical 'experiments' while exploring maximum information regarding the system. It is a spherical design having all the points of the sphere situated within the radius of $\sqrt{2}$. It avoids the design points on the cubical domain's vertices created by each variable's extreme values (Chen and Liu, 2018). Table 2 presents the input parameters and their initial values used in the analysis. These output parameters are represented in Table 3. A total of 25 numerical experiments were run using the DoE module of the ANSYS WB for various combinations of the input parameters. Output parameters such as von-Mises equivalent stress, directional deformation, the minimum number of cycles and minimum fatigue safety factor were determined for various combinations of input parameters. Table 4 presents the array of numerical experiments representing the data obtained by BBD and FEM. This data set was used to visualise the results in various graphs and contours.

Table 2 Input parameters used in the present experimental design

S. no.	*Name*	*Identification code*	*Initial value (mm)*
1	Bend radius	P1	5
2	Distance between holes	P6	20
3	Internal thickness	P11	1
4	External thickness	P12	1

Table 3 Output parameters used in the present experimental design

S. no.	*Name*	*Identification code*
1	Life minimum	P14
2	Safety factor minimum	P16
3	Directional deformation minimum	P17
4	Equivalent stress maximum	P18

Table 4 Box-Behnken DoE array

Numerical experiment #	*P1*	*P6*	*P11*	*P12*	*P14*	*P16*	*P17*	*P18*
1	5	20	1	1	129,463.2579	0.670717482	–1.083637595	257.0381787
2	4.5	18	1	1	159,851.9058	0.710853043	–0.940604568	242.5255146
3	5.5	18	1	1	85,981.60921	0.599442545	–1.322513938	287.6005407
4	4.5	22	1	1	170,167.9986	0.723212757	–0.877455533	238.3807508
5	5.5	22	1	1	96,041.09718	0.617797437	–1.235906243	279.055868
6	5	20	0.9	0.9	71,311.56943	0.569640091	–1.479393125	302.6472378
7	5	20	1.1	0.9	134,832.3271	0.678271993	–1.081730127	254.1753188
8	5	20	0.9	1.1	135,160.7364	0.678726956	–1.085594535	254.0049405
9	5	20	1.1	1.1	309,398.2933	0.815666836	–0.81807524	211.3608061
10	4.5	20	1	0.9	135,672.2456	0.679433985	–1.056374907	253.7406193
11	5.5	20	1	0.9	73,688.70164	0.574754694	–1.487300277	299.9540533
12	4.5	20	1	1.1	340,332.3179	0.829278924	–0.787967384	207.8914524
13	5.5	20	1	1.1	148,465.1945	0.696520406	–1.108298063	247.5160792
14	5	18	0.9	1	91,054.74786	0.608883676	–1.305443525	283.14111
15	5	22	0.9	1	86,669.00227	0.600745123	–1.218875527	286.9769448
16	5	18	1.1	1	155,249.9764	0.705152504	–0.969846249	244.4861205
17	5	22	1.1	1	183,147.0852	0.738014533	–0.905386209	233.5997359
18	4.5	20	0.9	1	143,485.8452	0.690001695	–1.058638811	249.8544588
19	5.5	20	0.9	1	66,902.42009	0.559815288	–1.489493012	307.9587207
20	4.5	20	1.1	1	349,153.4444	0.832972696	–0.786280274	206.9695693
21	5.5	20	1.1	1	157,572.77	0.708044888	–1.106662869	243.4873875
22	5	18	1	0.9	89,892.40177	0.606755002	–1.303302407	284.134452
23	5	22	1	0.9	90,321.32192	0.607542828	–1.216529012	283.7660033
24	5	18	1	1.1	161,081.342	0.712355823	–0.971440375	242.0138848
25	5	22	1	1.1	187,765.1226	0.743097631	–0.907135785	232.0018162

Figure 5 CAD model of the spring plate showing initial values of input parameters (see online version for colours)

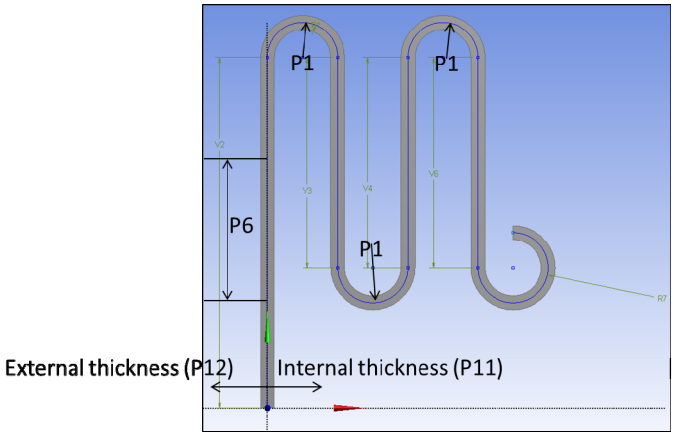

4 Results and discussion

4.1 Finite element analysis

Figure 6 shows the von Mises stress distribution in the structural steel spring plates for an applied static load of 35 N. The location of the highest stress is also shown in figure Both aluminium and steel spring plates are subjected to nearly identical equivalent stresses. As expected, the highest stress occurs at the top polar location of the upper hole. The regions below the upper hole and near the free end are subjected to minimum stresses minimising the probability of failure. Overall, the top polar location of the upper hole is identified as the critical location.

Figure 6 Von-Mises stress contours in the spring plate (see online version for colours)

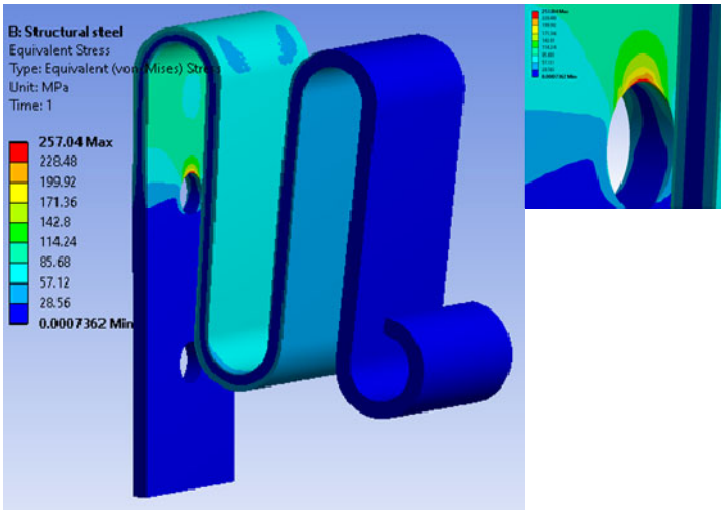

Figure 7(a) shows the minimum fatigue safety factor under the loading and boundary conditions presented in the section. The minimum safety factor in the spring plate was 0.67, observed in the polar location of the upper hole. Moreover, the area in the vicinity of the upper hole has a much lesser minimum factor of safety (pale yellow) compared to the regions away (blue). This observation indicates the higher probability of failure in the vicinity of the upper hole under uncertain loading scenarios. Figure 7(b) shows the minimum number of cycles completed by the steel spring plates before failure. The spring plate completed 1.2946×10^5 cycles prior to failure. In order to quantify the amount of damage caused, the ratio of maximum design cycles (1×10^9) and minimum life was expressed as the damage ratio. The spring plate manifested damage of 7907 under the fatigue loading.

Figure 7 (a) Minimum fatigue safety factor (b) Fatigue life contours in the spring plate (see online version for colours)

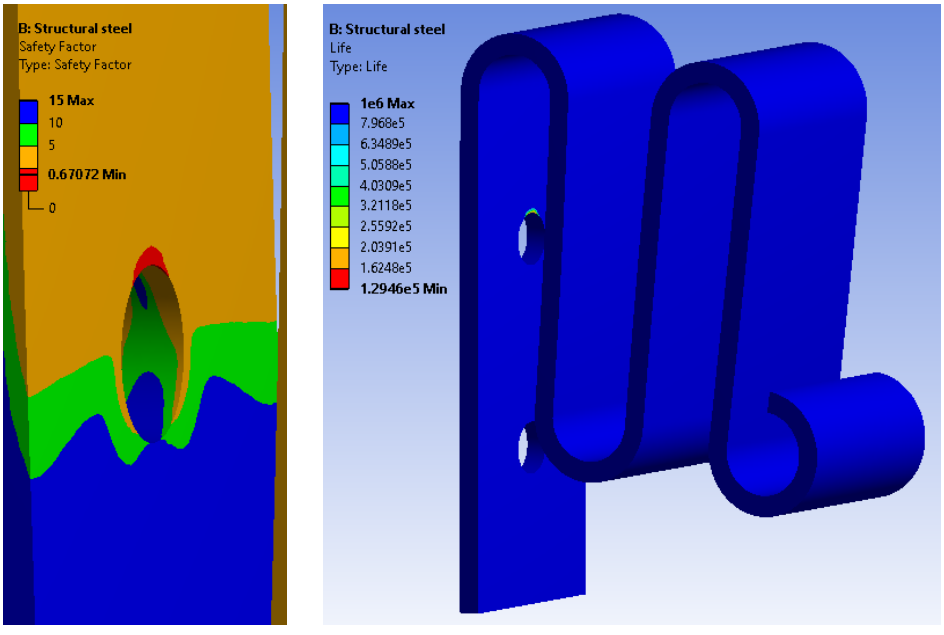

(a) (b)

The fatigue sensitivity curves obtained by plotting available life versus loading history for both types of spring plates are presented in Figure 8. As the load is reduced by 50%, the plate sustains 1×10^6 cycles. Interestingly, the available life 'plateau' up to 66.67% of the initial load is evident from the sensitivity curve for steel plate. This plateau indicates no loss in available life as the life is increased from 50% to 66.67% loading, as evident from the percentage reduction in the life curve. On the other hand, 47.44% of the spring plate life was lost as the load was increased from 50% to 70.83%. Also, when the load was increased to 104.17%, a 90.32% reduction in the available life was observed. This observation indicates a high failure probability with just a 4.17% increase in the loading.

Figure 8 Fatigue sensitivity and percentage reduction in life of spring plates (see online version for colours)

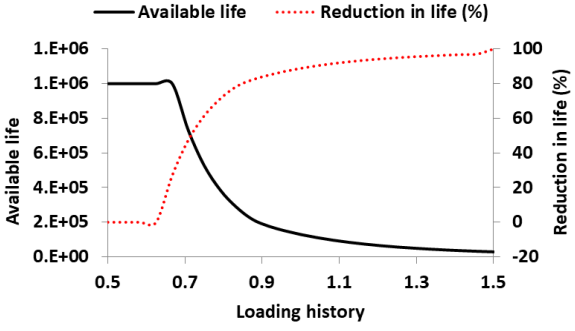

4.2 Statistical analysis

4.2.1 Goodness of fit

The statistical analysis of results was performed to understand the output parameters' response to changes in the input parameters. Figure 9 presents the goodness of fit between values determined from the FE model and those predicted by the RSM. It can be observed that both these values are in good agreement with each other. In order to develop equations for predicting the output parameters from the input parameters, regression analysis was performed using Minitab 19.

Figure 9 Goodness of fit between predicted and observed values for the spring plate (see online version for colours)

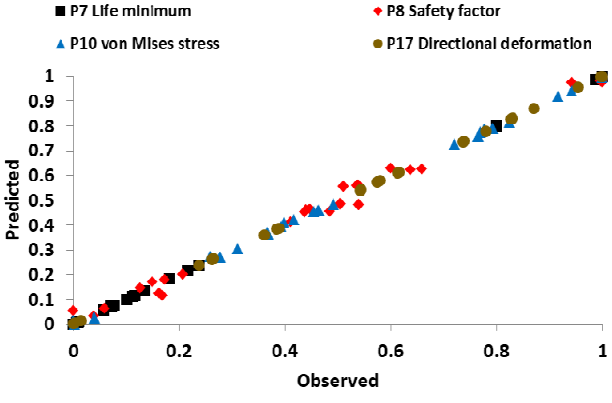

4.2.2 Regression analysis and ANOVA

The regression analysis and ANOVA were conducted to understand the effect of various input parameters on the output parameters. Equations (1) to (8) present the regression equations and the corresponding ANOVA tables. The linear regression equations express the output parameters in terms of the input parameters and coefficients. On the other hand, the ANOVA table was used mainly to ascertain the percentage contribution by each

parameter along with the percentage error. The percentage error is used to check the degree of validity of the regression equation. For clear understanding, the input parameters were categorised into groups: A: P1 and P6 and B: P11 and P12.

Equation (1) presents the linear regression model for the parameter, minimum life (P14) in terms of bend radius and (P1) and distance between holes (P6). Table 4 presents the corresponding ANOVA table for parameters P14, P1 and P6. It can be seen that the parameter P1 contributes 91.95% to the P14 compared to P6, which contributes just 2.56%. The error was obtained as 5.49%, manifesting the model's good accuracy. Similarly, equation (2) presents the linear regression model for P14 expressed as a function of the internal thickness (P11) and external thickness (P12). ANOVA for output parameter P14 and input parameters P11 and P11 is presented in Table 5. The parameters P11 and P12 have approximately equal contributions of 47.78% and 46.51%, respectively, resulting in an error of just 5.70%.

$$P14 = 458875 - 77419P1 + 3233P6 \tag{1}$$

Table 4 ANOVA table for P14, P1 and P6

Source	*DF*	*Seq SS*	*Contribution*	*Adj SS*	*Adj MS*	*F-Value*	*P-value*
Regression	2	3.47620E+11	94.51%	3.47620E+11	1.73810E+11	5,356.44	0.000
P1 – R1 (mm)	1	3.38186E+11	91.95%	3.38186E+11	3.38186E+11	10,422.15	0.000
P6 – dist_holes (mm)	1	9434157367	2.56%	9,434,157,367	9,434,157,367	290.74	0.000
Error	622	20183149257	5.49%	20,183,149,257	32,448,793		
Total	624	3.67803E+11	100.00%				

$$P14 = -818243 + 483942P11 + 477451P12 \tag{2}$$

Table 5 ANOVA table for P14, P11 and P12

Source	*DF*	*Seq SS*	*Contribution*	*Adj SS*	*Adj MS*	*F-value*	*P-value*
Regression	2	1.04307E+12	94.30%	1.04307E+12	5.21533E+11	5,141.28	0.000
P11 – FD2 (mm)	1	5.28575E+11	47.78%	5.28575E+11	5.28575E+11	5,210.70	0.000
P12 – FD3 (mm)	1	5.14491E+11	46.51%	5.14491E+11	5.14491E+11	5,071.86	0.000
Error	622	63,095,860,306	5.70%	63,095,860,306	101,440,290		
Total	624	1.10616E+12	100.00%				

Equation (3) presents the linear regression equation for the parameter P16 in terms of parameters P1 and P6. Table 6 presents the ANOVA table for the parameters P16, P1 and P6, specifying the percentage contribution. The table shows that P6 has a significantly high contribution of 94.13% in deciding the minimum safety factor of the spring plate (P14). On the other hand, P6 has a negligible contribution of just 1.60%. As a result, the error was only 4.27%, establishing the regression model's validity. Equation (4) presents the linear regression equation for the parameter P16 in terms of parameters P11 and P12.

Table 7 presents the ANOVA table for the parameters P16, P11 and P12. The parameters P11 and P12 contribute 50.28% and 48.73% in deciding the minimum safety factor, along with an error of just 0.99%. This value is slightly higher than that obtained for the minimum life.

$$P16 = 1.16665 - 0.114306(P1) + 0.003726(P6) \tag{3}$$

Table 6 ANOVA table for P16, P1 and P6

Source	*DF*	*Seq SS*	*Contribution*	*Adj SS*	*Adj MS*	*F-value*	*P-value*
Regression	2	0.74976	95.73%	0.74976	0.374880	6,974.64	0.000
P1-R1 (mm)	1	0.73722	94.13%	0.73722	0.737225	13,716.08	0.000
P6 – dist_holes (mm)	1	0.01253	1.60%	0.01253	0.012534	233.20	0.000
Error	622	0.03343	4.27%	0.03343	0.000054		
Total	624	0.78319	100.00%				

$$P16 = -0.58779 + 0.63803(P11) + 0.62813(P12) \tag{4}$$

Table 7 ANOVA table for P16, P11 and P12

Source	*DF*	*Seq SS*	*Contribution*	*Adj SS*	*Adj MS*	*F-value*	*P-value*
Regression	2	1.80924	99.01%	1.80924	0.904619	31,178.23	0.000
P11 – FD2 (mm)	1	0.91877	50.28%	0.91877	0.918769	31,665.91	0.000
P12 – FD3 (mm)	1	0.89047	48.73%	0.89047	0.890470	30,690.56	0.000
Error	622	0.01805	0.99%	0.01805	0.000029		
Total	624	1.82729	100.00%				

Equation (5) presents the regression equation for minimum deformation (P17) in terms of the parameters P1 and P6. Table 8 presents the ANOVA for parameter P17 w.r.t. parameters P1 and P6. Again, P1 and P6 contribute 95.41% and 4.44%, with an error of 0.15%. The regression model for P17 in terms of P1 and P6 is presented in equation (6). The ANOVA for P17, P11 and P12 is presented in Table 9. As shown in Table 9, the contribution of P11 and P12 was almost equal at 50.09% and 48.91%, respectively, with an error of 1%.

$$P17 = 0.37542 - 0.373374(P1) + 0.20148(P6) \tag{5}$$

Table 8 ANOVA table for P17, P1 and P6

Source	*DF*	*Seq SS*	*Contribution*	*Adj SS*	*Adj MS*	*F-value*	*P-value*
Regression	2	8.23237	99.85%	8.23237	4.11618	212,065.48	0.000
P1-R1 (mm)	1	7.86590	95.41%	7.86590	7.86590	405,250.80	0.000
P6 – dist_holes (mm)	1	0.36646	4.44%	0.36646	0.36646	18,880.16	0.000
Error	622	0.01207	0.15%	0.01207	0.00002		
Total	624	8.24444	100.00%				

$$P17 = -4.3857 + 1.65462P11 + 1.63495P12 \tag{5}$$

Table 9 ANOVA table for P17, P11 and P12

Source	*DF*	*Seq SS*	*Contribution*	*Adj SS*	*Adj MS*	*F-value*	*P-value*
Regression	2	12.2119	99.00%	12.2119	6.10595	30,939.67	0.000
P11 – FD2 (mm)	1	6.1790	50.09%	6.1790	6.17897	31,309.63	0.000
P12 – FD3 (mm)	1	6.0329	48.91%	6.0329	6.03294	30,569.70	0.000
Error	622	0.1228	1.00%	0.1228	0.00020		
Total	624	12.3347	100.00%				

The regression model for maximum von-Mises stress (P18) in parameters P1 and P6 is presented in equation (7). As shown in Table 10, the parameters P1 and P6 have 95.12% and 1.07% contribution in deciding the von-Mises stress amounting to an error of just 3.82%. Next, equation (8) presents the regression model for P18 in terms of parameters P11 and P12. Finally, the ANOVA table for P18 in terms of parameters P11 and P12 is presented in Table 11. Again, both input parameters (P11 and P12) have equal contributions of 50.88% and 48.95%, with an error of 0.17%.

$$P18 = 54.41 + 45.668P1 - 1.2104P6 \tag{7}$$

Table 10 ANOVA table for P18, P1 and P6

Source	*DF*	*Seq SS*	*Contribution*	*Adj SS*	*Adj MS*	*F-value*	*P-value*
Regression	2	119,000	96.18%	119,000	59,500	7,839.44	0.000
P1-R1 (mm)	1	117,678	95.12%	117,678	117,678	15,504.61	0.000
P6 – dist_holes (mm)	1	1,323	1.07%	1,323	1,323	174.27	0.000
Error	622	4,721	3.82%	4,721	8		
Total	624	123,721	100.00%				

$$P18 = 723.029 - 235.719(P11) - 231.199(P12) \tag{8}$$

Table 11 ANOVA table for P18, P11 and P12

Source	*DF*	*Seq SS*	*Contribution*	*Adj SS*	*Adj MS*	*F-value*	*P-value*
Regression	2	246,044	99.83%	246,044	123,022	183,823.08	0.000
P11 – FD2 (mm)	1	125,404	50.88%	125,404	125,404	187,382.02	0.000
P12 – FD3 (mm)	1	120,640	48.95%	120,640	120,640	180,264.14	0.000
Error	622	416	0.17%	416	1		
Total	624	246,460	100.00%				

4.2.3 Local sensitivity analysis

Figures 10(a) to 10(d) shows the local sensitivity curves for the output (P14, P15, P16, P17 and P18) and input parameters (P1, P6, P11 and P12). As shown in Figures 10(a) and 10(b), the parameters P14 and P16 decrease with an increase in P1 and increases with an increase in P11 and P12. The coincidence of P11 and P12 corroborate with the nearly equal contribution of these two factors observed in ANOVA. For both the parameters, P14 and P16, the parameter P6 has minor sensitivity as indicated by the change in its

value w.r.t. input parameters. Figures 10(c) and 10(d) present the sensitivity of parameters P17 and P18 w.r.t. the input parameters. From Figure 10(c) shows a steep linear increase in P17 with P1, indicating a strong relationship between them. However, this increase is less steep in parameter P18 [see Figure 10(d)]. On the other hand, parameters P6 have an inverse relationship with both P17. As can be seen from Figure 10(d), the effect of P6 is negligible on P18. As obviously, both P17 and P18 decrease with the increase in the parameters P11 and P12 as the spring plate thickness increases.

Figure 10 Local sensitivity curves for the output parameters w.r.t. input parameters (see online version for colours)

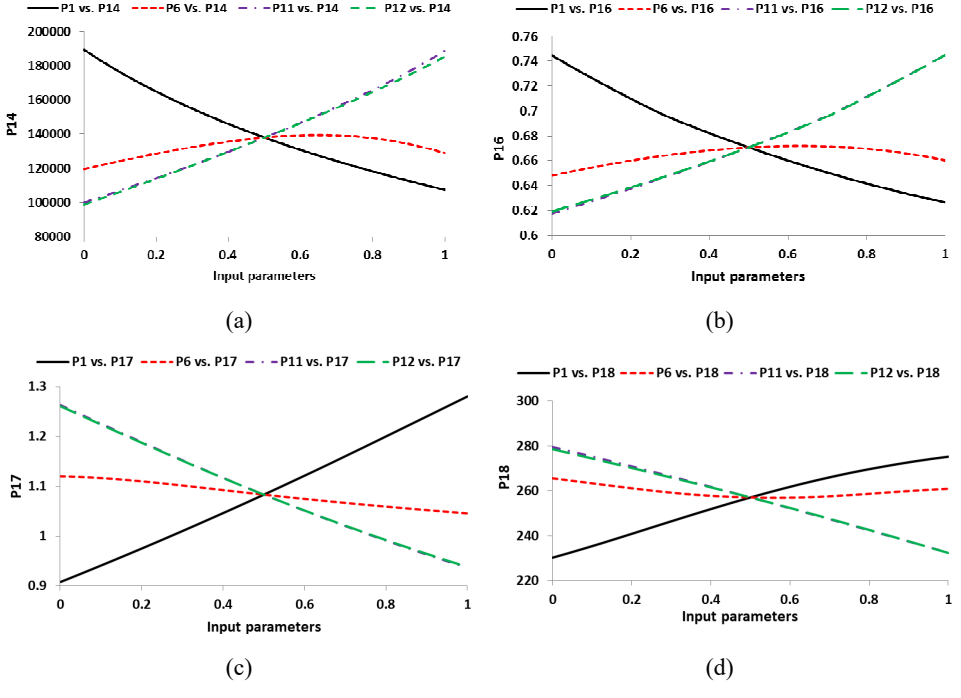

4.2.4 Response surface contour plots

The contour plots obtained from RSM were employed to gain further insight into the relationship between input and output parameters. Figures 11(a) to 11(h) presents these contour plots, which can be used to identify the trend of output parameters w.r.t. change in the input parameters. Figure 11(a) shows the contour plot for P14 w.r.t. P1 and P6. The minimum number of life (P14) is highest for the combination of smaller values of P1. The dark region corresponds to values of P6 ranging between 19 mm and 22 mm, and the minimum values of P1 correspond to 180,000 cycles before failure. On the other hand, the smallest value of minimum life (<100,000) occurs at the region corresponding to higher values of P1 and lower values of P6. Figure 11(b) presents the contour plots for the P14 w.r.t. internal and external thicknesses (P11 and P12, respectively). As expected, the maximum values of P14 occur at the highest P11 and P12. At maximum P11 and P12, the spring plate is expected to complete 300,000 cycles before failure. Figure 11(c) shows

the dependence of the minimum safety factor (P16) upon the parameters P1 and P6. Again, the maximum value of P16 (>0.74) occurs at the minimum value of P1. On the other hand, as shown in Figure 11(d), the maximum value of P16 (>0.80) occurs at the region corresponding to the highest value of P11 and P12. As shown in Figure 11(e), the maximum value of P18 (>280 MPa) occurs for the highest value of P1 and the lowest value of P6. On the other hand, as expected, the maximum value of P18 (>280 MPa) occurs for the minimum thicknesses, i.e. P11 and P12 [see Figure 11(f)]. Figure 11(g) shows the variation of P17 with the P1 and P6. The dark region corresponding to P17 > –0.9 occurs at the highest value of P1 and the lowest value of P6. On the other hand, the region corresponding to P < –1.4 occurs for the minimum values of P11 and P12 [Figure 11(h)].

Figure 11 Contour plots for various input and output parameters (see online version for colours)

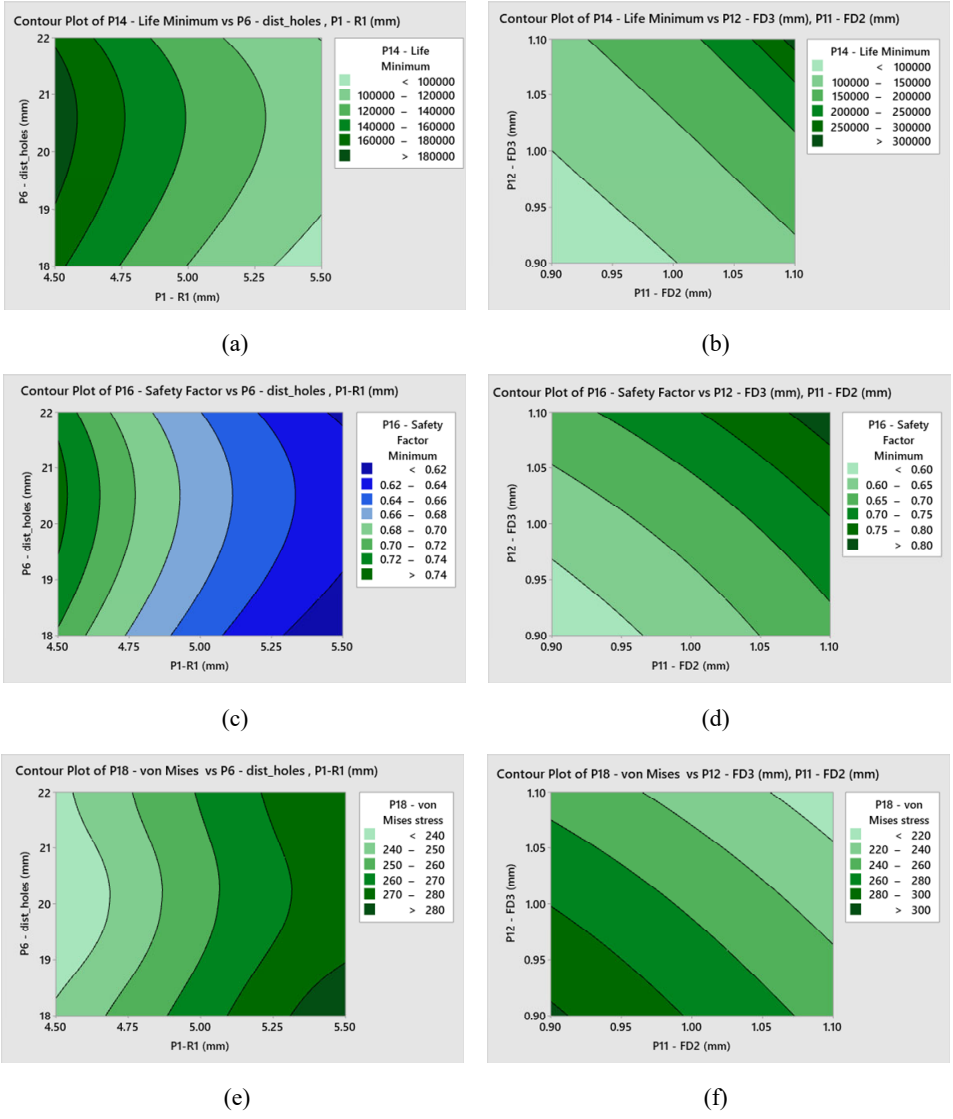

Figure 11 Contour plots for various input and output parameters (continued) (see online version for colours)

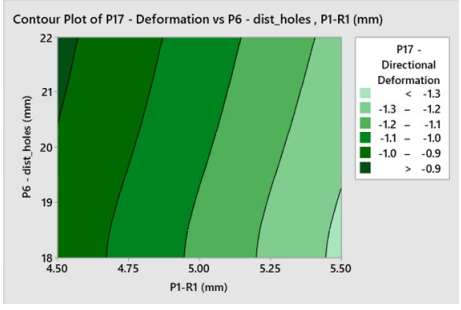

(g)

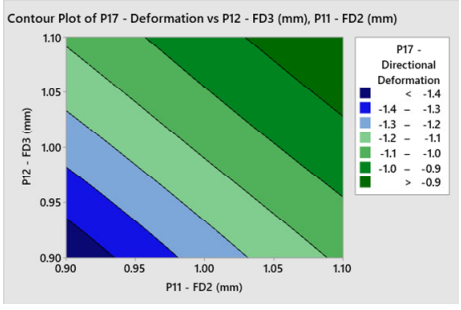

(h)

5 Conclusions

The present study deals with the design exploration of a structural spring plate using the combination of DoE and FEM. The spring plate was meshed with 265,894 tetrahedral finite elements and subjected to a load of 35N. The FE model was then employed to obtain the maximum deformation and von Mises stress through static analysis. A zero-based fatigue analysis with Goodman mean correction was performed to ascertain its fatigue life. The fatigue sensitivity analysis revealed a 47.44% and 90.32% loss in fatigue life, with an increase in load from 70.83% and 104.17%, respectively. The BBD methodology was employed for the design exploration and RSM for four input and output parameters. The goodness of fit analysis revealed good agreement between output values predicted by the RSM and those obtained through FEM.

Further, linear regression analysis and ANOVA was performed to determine the relationship between input and output parameters and the percentage contribution of various factors. It was revealed that out of all factors considered, P1 has the highest contribution, followed by P11 and P12 and P6. The maximum regression model error was 5.70% establishing the general validity of the regression models. Finally, the local sensitivity analysis and RSM were performed to reveal the effect of change in various input parameters on the output parameters.

References

Al-Momani, E. and Rawabdeh, I. (2008) 'An application of finite element method and design of experiments in the optimization of sheet metal blanking process', *JJMIE*, Vol. 2, No. 1, pp.53–63.

Amanov, A., Karimbaev, R., Maleki, E., Unal, O., Pyun, Y.S. and Amanov, T. (2019) 'Effect of combined shot peening and ultrasonic nanocrystal surface modification processes on the fatigue performance of AISI 304', *Surface and Coatings Technology*, Vol. 358, No. 1, pp.695–705.

Antunes, R.A. and de Oliveira, M.C.L. (2012) 'Corrosion fatigue of biomedical metallic alloys: mechanisms and mitigation', *Acta Biomaterialia*, Vol. 8, No. 3, pp.937–962.

Bin Kamarudin, M.N., Mohamed Ali, J.S., Aabid, A. and Ibrahim, Y.E. (2022) 'Buckling analysis of a thin-walled structure using finite element method and design of experiments', *Aerospace*, Vol. 9, No. 10, p.541.

Bordonaro, G., Leardi, R., Diviani, L. and Berto, F. (2018) 'Design of experiment as a powerful tool when applying finite element method: a case study on prediction of hot rolling process parameters', *Frattura ed Integrità Strutturale*, Vol. 44, No. 12, pp.1–15.

Chen, X. and Liu, Y. (2018) *Finite Element Modeling and Simulation with ANSYS Workbench*, CRC Press, Boca Raton, Florida.

Connolly, M., Martin, M., Amaro, R., Slifka, A. and Drexler, E. (2019) 'Hydrogen isotope effect on the embrittlement and fatigue crack growth of steel', *Materials Science and Engineering: A*, Vol. 753, pp.331–340.

Das, S.K., Mukhopadhyay, N.K., Kumar, B.R. and Bhattacharya, D.K. (2007) 'Failure analysis of a passenger car coil spring', *Engineering Failure Analysis*, Vol. 14, No. 1, pp.158–163.

Ertas, A.H. and Sonmez, F.O. (2008) 'A parametric study on fatigue strength of spot-weld joints', *Fatigue & Fracture of Engineering Materials & Structures*, Vol. 31, No. 9, pp.766–776.

Gianchandani, Y.B. and Crary, S.B. (1998) 'Parametric modeling of a microaccelerometer: comparing I-and D-optimal design of experiments for finite-element analysis', *Journal of Microelectromechanical Systems*, Vol. 7, No. 2, pp.274–282.

Guo, S., He, Y., Shi, L., Pan, S., Tang, K., Xiao, R. and Guo, P. (2017) 'Modal and fatigue analysis of critical components of an amphibious spherical robot', *Microsystem Technologies*, Vol. 23, No. 6, pp.2233–2247.

Guo, T., Liu, Z., Correia, J. and de Jesus, A.M. (2020) 'Experimental study on fretting-fatigue of bridge cable wires', *International Journal of Fatigue*, Vol. 131, No. 1, p.105321.

Ijagbemi, C.O., Oladapo, B.I., Campbell, H.M. and Ijagbemi, C.O. (2016) 'Design and simulation of fatigue analysis for a vehicle suspension system (VSS) and its effect on global warming', *Procedia Engineering*, Vol. 159, pp.124–132.

Kong, Y.S., Omar, M.Z., Chua, L.B. and Abdullah, S. (2014) 'Fatigue life prediction of parabolic leaf spring under various road conditions', *Engineering Failure Analysis*, Vol. 46, No. 1, pp.92–103.

Kraus, C., Falk, T., Mauermann, R. and Drossel, W.G. (2020) 'Development of a new self-flaring rivet geometry using finite element method and design of experiments', *Procedia Manufacturing*, Vol. 47, pp.383–388.

Kumar, M.S. and Vijayarangan, S. (2007) 'Analytical and experimental studies on fatigue life prediction of steel and composite multi-leaf spring for light passenger vehicles using life data analysis', *Materials Science*, Vol. 13, No. 2, pp.141–146.

Li, S., Liu, X., Wang, X. and Wang, Y. (2019) 'Fatigue life prediction for automobile stabilizer bar', *International Journal of Structural Integrity*, Vol. 11, No. 2, pp.303–323.

Liu, F., Chen, Y., He, C., Wang, C., Li, L., Liu, Y. and Wang, Q. (2021) 'Very long life fatigue failure mechanism of electron beam welded joint for titanium alloy at elevated temperature', *International Journal of Fatigue*, Vol. 152, No. 1, p.106446.

Liu, F., Zhang, H., Liu, H., Chen, Y., Muhammad Kashif, K., Wang, Q. and Liu, Y. (2019) 'Influence of welded pores on very long-life fatigue failure of the electron beam welding joint of TC17 titanium alloy', *Materials*, Vol. 12, No. 11, p.1825.

Lu, Y., Ripplinger, K., Huang, X., Mao, Y., Detwiler, D. and Luo, A.A. (2019) 'A new fatigue life model for thermally-induced cracking in H13 steel dies for die casting', *Journal of Materials Processing Technology*, Vol. 271, pp.444–454.

Ma, L., Fong, J., Lane, B., Moylan, S., Filliben, J., Heckert, A. and Levine, L. (2015) 'Using design of experiments in finite element modeling to identify critical variables for laser powder bed fusion', in *2014 International Solid Freeform Fabrication Symposium*, University of Texas at Austin.

Maleki, E. and Unal, O. (2018) 'Roles of surface coverage increase and re-peening on properties of AISI 1045 carbon steel in conventional and severe shot peening processes', *Surfaces and Interfaces*, Vol. 11, No. 1, pp.82–90.

Parida, A.K. and Maity, K.P. (2016) 'Finite element method and experimental investigation of hot turning of Inconel 718', in *Advanced Engineering Forum*, Vol. 16, No. 1, pp.24–32, Trans Tech Publications Ltd.

Pastorcic, D., Vukelic, G. and Bozic, Z. (2019) 'Coil spring failure and fatigue analysis', *Engineering Failure Analysis*, Vol. 99, No. 1, pp.310–318.

Prasanna Naveen Kumar, J., Johns Kumar, S., Sarathi Jeyathilak, R.K., Venkatesh, M., Simon Christopher, A. and Ganesh, K.C. (2017) 'Effect of design parameters on the static mechanical behaviour of metal bellows using design of experiment and finite element analysis', *International Journal on Interactive Design and Manufacturing (IJIDEM)*, Vol. 11, No. 3, pp.535–545.

Prawoto, Y., Ikeda, M., Manville, S.K. and Nishikawa, A. (2008) 'Design and failure modes of automotive suspension springs', *Engineering Failure Analysis*, Vol. 15, No. 8, pp.1155–1174.

Ren, P.R., Song, W., Zhong, G., Huang, W.Q., Zuo, Z.X., Zhao, C.Z. and Yan, K.J. (2021) 'High-cycle fatigue failure analysis of cast Al-Si alloy engine cylinder head', *Engineering Failure Analysis*, Vol. 127, No. 1, p.105546.

Schäfer, C. and Finke, E. (2008) 'Shape optimisation by design of experiments and finite element methods – an application of steel wheels', *Structural and Multidisciplinary Optimization*, Vol. 36, No. 5, pp.477–491.

Senalp, A.Z., Kayabasi, O. and Kurtaran, H. (2007) 'Static, dynamic and fatigue behavior of newly designed stem shapes for hip prosthesis using finite element analysis', *Materials & Design*, Vol. 28, No. 5, pp.1577–1583.

Shuaeib, F.M., Hamouda, A.M.S., Wong, S.V., Umar, R.R. and Ahmed, M.M. (2007) 'A new motorcycle helmet liner material: The finite element simulation and design of experiment optimization', *Materials & Design*, Vol. 28, No. 1, pp.182–195.

Wei, C. and Olatunbosun, O.A. (2016) 'The effects of tyre material and structure properties on relaxation length using finite element method', *Materials & Design*, Vol. 102, No. 1, pp.14–20.

Yang, K., Huang, Q., Wang, Q. and Chen, Q. (2020) 'Competing crack initiation behaviors of a laser additively manufactured nickel-based superalloy in high and very high cycle fatigue regimes', *International Journal of Fatigue*, Vol. 136, No. 1, p.105580.

Zarrin-Ghalami, T. and Fatemi, A. (2013) 'Fatigue life predictions of rubber components: Applications to an automobile cradle mount', *Proceedings of the Institution of Mechanical Engineers, Part D: Journal of Automobile Engineering*, Vol. 227, No. 5, pp.691–703.

Zenner, H. and Hinkelmann, K. (2019) 'August Wöhler–founder of fatigue strength research: On the 200th anniversary of August Wöhler's birth', *Steel Construction*, Vol. 12, No. 2, pp.156–162.

Zerbst, U. and Klinger, C. (2019) 'Material defects as cause for the fatigue failure of metallic components', *International Journal of Fatigue*, Vol. 127, No. 1, pp.312–323.

Zhan, Z. (2019) 'Experiments and numerical simulations for the fatigue behavior of a novel TA2-TA15 titanium alloy fabricated by laser melting deposition', *International Journal of Fatigue*, Vol. 121, No. 1, pp.20–29.

Zhang, P., Wang, D., Guo, Y., Cheng, P., Shao, C., Lang, N., Liu, X. and Huang, J. (2021) 'Fatigue failure analysis and finite element assessment of the twin torsion spring', *Engineering Failure Analysis*, Vol. 122, No. 1, p.105187.

Zhu, Y., Wang, Y. and Huang, Y. (2014) 'Failure analysis of a helical compression spring for a heavy vehicle's suspension system', *Case Studies in Engineering Failure Analysis*, Vol. 2, No. 2, pp.169–173.